Materials Today Energy 25 (2022) 100979

Contents lists available at ScienceDirect

Materials Today Energy

journal homepage: www.journals.elsevier.com/materials-today-energy/

Safe extended-range cycling of $Li_4Ti_5O_{12}$-based anodes for ultra-high capacity thin-film batteries

Valerie Siller [a], Juan Carlos Gonzalez-Rosillo [a], Marc Nuñez Eroles [a], Michel Stchakovsky [b], Raul Arenal [c, d, e], Alex Morata [a, **], Albert Tarancón [a, f, *]

[a] Catalonia Institute for Energy Research (IREC), Jardins de Les Dones de Negre 1, Planta 2, Sant Adrià Del Besòs, 08930, Barcelona, Spain
[b] HORIBA Scientific, 14 Boulevard Thomas Gobert, Passage Jobin Yvon, 91120, Palaiseau, France
[c] Instituto de Nanociencia y Materiales de Aragon (INMA), CSIC-Universidad de Zaragoza, Calle Pedro Cerbuna, 50009, Zaragoza, Spain
[d] Laboratorio de Microscopias Avanzadas (LMA), Universidad de Zaragoza, Calle Mariano Esquillor, 50018, Zaragoza, Spain
[e] Fundacion ARAID, 50018, Zaragoza, Spain
[f] Catalan Institution for Research and Advanced Studies (ICREA), Passeig Lluís Companys 23, 08010, Barcelona, Spain

ARTICLE INFO

Article history:
Received 19 January 2022
Received in revised form
23 February 2022
Accepted 26 February 2022
Available online 4 March 2022

Keywords:
Microbatteries
Anode
Lithium titanium oxide
Operando spectroscopic ellipsometry
Pulsed laser deposition

ABSTRACT

Lithium titanium oxide thin films are increasingly popular anode materials in microbatteries and hybrid supercapacitors, due to their improved safety, cost, and cycle lifetime. So far, research efforts have mainly focused on the pure spinel phase $Li_4Ti_5O_{12}$ (LTO) and only a small fraction is dedicated to a broader spectrum of titanium-based metal oxide thin films. In this work, pulsed laser deposition is used in a multilayer approach by alternating LTO and Li_2O ablations to create a heterogeneous landscape in the titania-based micro-anodes. This rich microstructure enables the safe extension of the accessible electrochemical window down to 0.2 V. This leads to extraordinary high specific capacities of 250–300 mAh/g at 1 C, maintaining a stable discharge capacity of 180 mAh/g at 16 C. *Operando* spectroscopic ellipsometry and Raman spectroscopy are used to track optical and structural changes as a function of the discharge voltage down to 0.01 V. A kinetically limited degradation mechanism based on the effective trapping of Li-ions at the octahedral 16c positions is proposed when cycling in the range of 0.2–0.01 V. In essence, our work contributes to titania-based nanoshapes as anodes of increased specific capacity due to a higher Li-site occupation, while maintaining their good stability and safety.

1. Introduction

The current state-of-the-art lithium-ion batteries face several safety issues and physicochemical limitations for reaching high power and energy densities, which is required for their application in novel autonomous microelectronic devices for the Internet-of-Things (IoT) [1,2]. On the other hand, the enormous expected growth in the number of sensor nodes and other IoT devices in the next decade imposes the development of sustainable micro-power sources, whose manufacturing process could be compatible with Si technology processing. Especially, the search for inexpensive battery anodes with a simple manufacturing process has become a major challenge.

Among other increasingly popular alternatives to metal Li anodes [3],titania-based electrodes, such as TiO_2 (rutile, anatase, and black titania) [4–7], Li_2TiO_3 [8], $Li_2Ti_3O_7$ [9], and $Li_4Ti_5O_{12}$, [10,11] are known to stably reduce Ti^{4+} to Ti^{3+} in a voltage range of 3.0–1.0 V vs. Li/Li^+ [12]. As a consequence, a great increase in device safety can be achieved and the application of high-voltage cathode materials is enabled [13]. The most studied phase is spinel $Li_4Ti_5O_{12}$, known as a "zero-strain" material with a very low lattice expansion of 0.2–0.3% in a two-phase reaction process between $Li_4Ti_5O_{12}$ and $Li_7Ti_5O_{12}$, a stable electrode/electrolyte interphase [14–17], and impressive rate capabilities, despite the rather low electronic and ionic conductivities of the end members [18,19]. The fairly poor transport properties can be ameliorated via aliovalent cation doping, non-stoichiometric oxygen defects, or a mixture with metallic secondary phases [13,20,21].

A second critical issue of LTO-based anodes is their low specific capacity of 175 mAh/g forming $Li_7Ti_5O_{12}$ at potentials above 1.0 V vs. Li/Li^+. It is generally accepted that a non-detrimental solid

* Corresponding author.
** Corresponding author.
E-mail addresses: amorata@irec.cat (A. Morata), atarancon@irec.cat (A. Tarancón).

https://doi.org/10.1016/j.mtener.2022.100979

electrolyte interphase (SEI) layer is formed (and dissolved) on top of LTO at high cut-off voltages, which in turn also prevents the LTO from degassing upon contact with the electrolyte [22]. The insertion of extra lithium into the LTO structure would have a large impact on the accessible capacity up to a theoretical value of 293 mAh/g, assuming every Ti^{4+} is reduced to Ti^{3+}. However, discharging to 0 V was reported to be unfavorable for the Li-ion diffusion beyond $Li_7Ti_5O_{12}$, which significantly increases polarization and reduces reaction kinetics [23]. An amorphous SEI layer ~10 nm is known to evolve when discharged at 0.01 V vs. Li/Li^+, which has been claimed to stabilize in subsequent charge and discharge cycles with capacities as high as 230 mAh/g. Yet, deeper insights into the structural consequences of cycling to very low potentials and assessment of the actual stability limits for the optimization of the accessible capacity are still missing.

The fabrication of such LTO thin films usually involves high vacuum deposition techniques [24], like RF sputtering [25], atomic layer deposition (ALD) [26], or pulsed laser deposition (PLD) [27,28]. A common problem across these techniques is the volatility of lithium during processing. Besides the usual overlithiation of the ceramic targets, a versatile approach based on multilayers or co-deposition with Li-rich targets (Li_2O and Li_3N) is found to be quickly emerging in the field [25,28] [–] [32]. In addition, this strategy can be used to fabricate nanocomposites comprising different materials [33]. While this approach is being successfully applied in the energy community [34], its application to the field of Li-ion batteries is still in its infancy [35]. Interestingly, LTO–TiO_2 composites have been suggested to have a positive impact on the specific capacity, stability at fast rates, and low potentials [16,36–41]. To the best of our knowledge, there are no reports in the literature to address this topic in detail.

In this work, we aim to implement the rapidly growing manufacturing process of alternating targets during the deposition in a large-area (LA) PLD to compensate Li-losses and to obtain a fine control over the phase landscape in LTO-based nanocomposite anodes of exceptional electrochemical performance. In addition, the structural implications of cycling to very low potentials are determined via *operando* spectroscopic ellipsometry (SE) and Raman spectroscopy and later included for discussion on the cyclability limits of the fabricated nanocomposites.

2. Materials and methods

2.1. Thin-film fabrication

Targets for thin-film depositions via PLD have been purchased from Neyco for $Li_4Ti_5O_{12}$ (99.9%) and from Codex for Li_2O (99.9%). Depositions have been carried out on $Si_{(100)}$-chips (1 × 1 cm) covered with SiO_2 (100 nm) and Si_3N_4 (300 nm) on both sides. To provide electrical accessibility of the anode thin films, one side of the substrate was sputtered with 10 nm titanium (adhesive layer) and 80 nm platinum (serving as backside contact of the thin films) on top. Substrates have been fabricated by the Institute of Microelectronics of Barcelona (IMB-CNM). Anode thin films are deposited in an LA PLD-5000 system from PVD products using a Coherent (Lambda Physik) COMPex PRO 205 KrF excimer laser (wavelength λ = 248 nm, pulse duration = 20 ns, maximum pulse energy = 700 mJ, and maximum repetition rate f = 50 Hz). A multilayering approach between LTO and Li_2O targets has been chosen in the PLD, which was previously described by *Fehse* et al. [31] for comparable spinel thin films (see more details in the Supporting Information Fig. S1). Different ratios of ablation pulses between LTO and Li_2O were realized during a controlled alternation of the targets inside the chamber. Ablation cycles have been repeated until the desired film thickness was reached. All thin films were deposited under a constant substrate-to-target distance of 90 mm, a substrate temperature of 650 °C, and a continuous rotation of substrates and targets. The partial background gas pressure (pO_2) was set to 20 mTorr with 5 sccm O_2 mass flow and the laser fluence was fixed at 1.3 J/cm^2 for all depositions.

2.2. Structural characterization

Scanning electron microscopy (SEM) imaging has been carried out with a ZEISS AURIGA equipped with a 30 kV Gemini FESEM column and an InLens detector. Structural analysis was performed in a PANalytical X'Pert PRO MRD diffractometer using a grazing incidence (GI) setup with Cu-Kα radiation (λ = 1.54184 Å) under an incident beam angle ω between 0.33° and 0.40° in a range of 2θ of 15–50° at the Scientific and Technological Center (CCiT) at the University of Barcelona. All measurements were collected under the same experimental conditions. Raman spectra were collected using a HORIBA Scientific Raman Superhead, coupled to an iHR320 monochromator equipped with a Syncerity CCD (1024 × 256, pixel size 26 μm × 26 μm) and a laser at λ = 532 nm (green), capable of a spectral range from 100 to 7700/cm (gratings available are 600, 1200, and 1800 lines/mm). A microscope objective of 0.90/100× was used with a resulting spot diameter of 721 nm. Pristine LTO thin films on Pt-covered substrates were mounted in an FEI Dual Beam Helios NanoLab 600 and thin-film lamellas (40–50 nm thickness) prepared across-plane with a focused Ga-ion beam. Scanning transmission electron microscopy (STEM) was carried out using a probe aberration-corrected ThermoFisher Scientific Titan Low-Base, equipped with a high-brightness field emission gun operating at 300 keV. Electron energy loss spectroscopy (EELS) has been conducted using the spectrum-imaging acquisition mode [42,43], minimizing possible damages of the material's structure with the electron beam. EEL spectra were recorded using a Gatan GIF Tridiem ESR 866 spectrometer. The convergent semi-angle was 25 mrad, the collection semi-angle was 10 mrad, the energy resolution was ~1.2 eV, the acquisition time for each spectrum was 0.08–0.1 s, and the energy dispersion was 0.5 eV/channel. Li K-edge, O K-edge, and Ti L-edge were employed to build EELS maps.

2.3. Spectroscopic ellipsometry

UVISEL+ phase modulation ellipsometry equipment by Horiba Scientific was used for acquiring the optical spectra. It is equipped with a UV xenon lamp and covers a spectral range of 0.6–4.8 eV (and 0.6–6.5 eV in a similar work station located at HORIBA France SAS, respectively). The incident beam angle was fixed to 70° and the beam spot size to 2 mm^2 on the sample surface. SE data have been fitted with the DeltaPsi2® software provided by Horiba France SAS, using a material model consisting of several (4–5) Tauc–Lorentz oscillators (see Eq. S4). Once the suitable material properties have been assigned, a model based on several overlayers, including the application of the Bruggeman Effective Medium Approximation (EMA), is implemented (see more details in the Supporting Information Fig. S5). For the *operando* measurements, an acquisition time of ~4 min/spectrum was employed. *Operando* SE was enabled through an air-tight in-situ chamber printed at IREC facilities with a Formlabs Form2® SLA 3D printer, using photopolymer resin based on methacrylate. The three-electrode setup was mounted in the air-tight optical chamber inside the glovebox, sealed, and moved outside to the SE station in ambient air.

2.4. Electrochemical measurements

Electrochemical measurements required the thin-film samples to be electrically connected on their backside Pt-contacts and

embedded in a robust dual-component resin to prevent any contact between current collectors and the liquid electrolyte. First ex-situ electrochemical characterization has been carried out in an Ar-filled glovebox with internal 0.1 ppm O_2 and 0.0 ppm H_2O levels. Thin films have been operated as working electrodes in a common three-electrode setup, with lithium as counter and reference electrodes, all together immersed in a 1 M $LiPF_6$ EC/DMC = 50/50 (v/v) battery grade (Sigma Aldrich) liquid electrolyte. Electrochemical measurements have been performed using the BioLogic SP-50 (Lambda System) potentiostat/galvanostat unit under the control of the EC-Lab® software collecting cyclic voltammetry and chronopotentiometry. The mass was calculated, assuming a fully dense lithium titanate layer. Given the uncertainty in the determination of the true density of the films, we acknowledge a 10% error in the estimation of the specific capacities reported.

3. Results and discussion

3.1. Structural and morphological characterization of the layers

LTO thin films were deposited by PLD multilayering, under increasing Li_2O addition, on top of $Si_3N_4/SiO_2/Si$ substrates with current collection capabilities (Pt/Ti). The evolution of their microstructure was studied by SEM (Fig. 1) for alternated ablation of LTO and Li_2O targets when different pulse ratios were selected, ranging from the sole ablation of the LTO plane target (Fig. 1a) to the ablation ratios of 2:1 (Figs. 1b) and 4:3 (Fig. 1c). A detailed description of the multilayer approach employed for the PLD deposition of the layers is provided in the Supporting Information Fig. S1.

Upon comparison of SEM images in Fig. 1(a–c) from LTO thin films with and without additional Li_2O, an increasing crystallization with greater Li content becomes evident. Particle sizes range on average from 100 nm for LTO to 150 nm for Li_2O-enriched LTO. The improved crystallinity leads to an enhanced microstructure of fewer grain boundaries, which typically represent an obstacle for ionic mass transport. Besides a certain grain growth, very small particles in the average size of 50 nm can be observed in all three layers. Cross-sectional images reveal dense layers of thicknesses around 146 nm, as shown in Fig. 1(d) for layers deposited at a pulse ratio of 2:1 for LTO:Li_2O. Remarkably, there is no visual trace of the multilayer PLD fabrication process, evidencing the merging of the Li_2O layers into the LTO ones, compensating Li-losses.

In Fig. 2, the structural evolution of the $Li_4Ti_5O_{12}$ spinel phase upon a staggered lithium addition in the PLD is analyzed with GI-XRD in (a) and Raman spectroscopy in (b).

Based on the X-ray diffractograms collected in grazing incidence (GI-XRD, Fig. 2a), the spinel phase of polycrystalline LTO can be identified by the characteristic (111) peak at $2\theta \approx 18.5^\circ$, which exhibits an increase in crystallinity with the progressive addition of Li_2O during the layer deposition. Further peaks corresponding to polycrystalline TiO_2-rutile and -anatase secondary phases can be assigned. The rutile phase appears to be present in all samples, decreasing for layers with a higher lithium content relative to the characteristic peak of LTO. Anatase shows a notable decrease with the higher addition of Li_2O. Another secondary phase occurs at $2\theta \approx 17.4^\circ$ when multilayering with a Li_2O target is implemented in the deposition procedure (see the orange asterisk in Fig. 2(a)), which did not allow an unambiguous assignment to any phase associated with LTO. Raman spectra in Fig. 2(b) reveal the main presence of anatase and rutile phases and no evidence of spinel LTO for lower lithium contents. With increasing Li_2O addition, the anatase signal vanishes and some vibrational modes of LTO become evident. Rutile appears to be present at any lithium concentration, which is in accordance with the phases identified by GI-XRD. The appearance of titania secondary phases is a typical consequence of lithium loss during the LTO deposition in the PLD [14,44]. Especially, nano-scaled TiO_2 shapes (anatase, rutile, and black titania) have increased the capabilities of lithium uptake for titania-based anodes and promoted their electrochemical activity and performance in lithium-ion batteries [4,5,7,45]. In this context, the role of titania nanoparticles in the multilayered LTO thin films is of special interest for the following analysis.

Elemental mapping has been conducted by STEM-EELS in cross-sections of the LTO thin films and is shown in Fig. 3 for depositions without (a) and with (b) additional Li_2O content for the region of interest (area marked by red dashed lines in the STEM high-angle annular dark-field (HAADF) image). A color code is applied to differentiate among Li (red), Ti (blue), and O (green). When comparing the sum of the elemental maps for pure LTO ablations and LTO:Li_2O (4:3) multilayers in Fig. 3(a) and (b) respectively, the greatest difference occurs in the oxygen signal. In Fig. 3(a), LTO is showing areas rich in Li and Ti, which are strongly

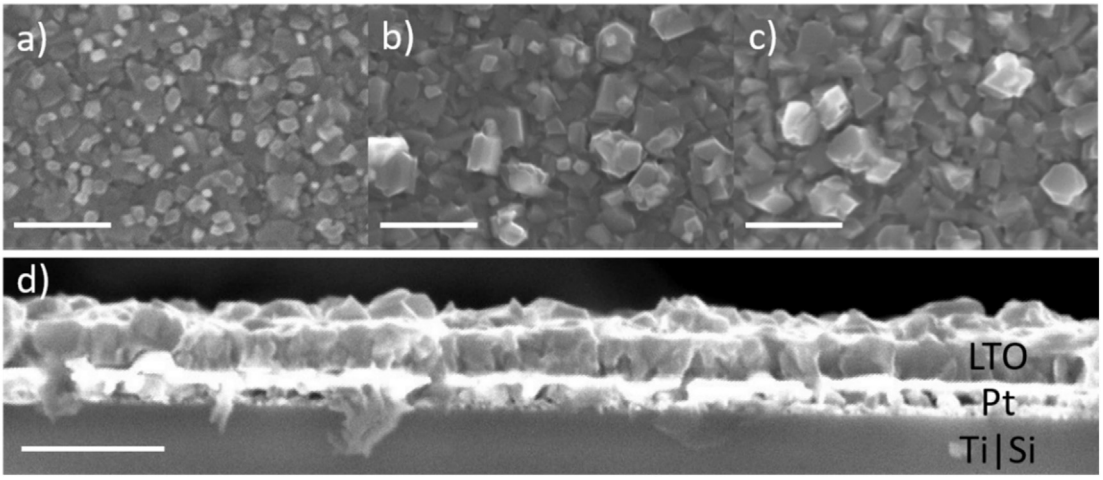

Fig. 1. SEM images of LTO thin films deposited as alternating multilayers of $Li_4Ti_5O_{12}$ and Li_2O by PLD. The pulse ratio of LTO:Li_2O is distributed as (a) 1:0, (b) 2:1, and (c) 4:3. In (d) the cross-section for the LTO thin film (2:1) is shown on top of the Pt current collector. The film thickness is ~146 nm and the white scale bar corresponds to 500 nm. The remaining substrate below the 80 nm sputtered Pt-layer is abbreviated as "Ti|Si".

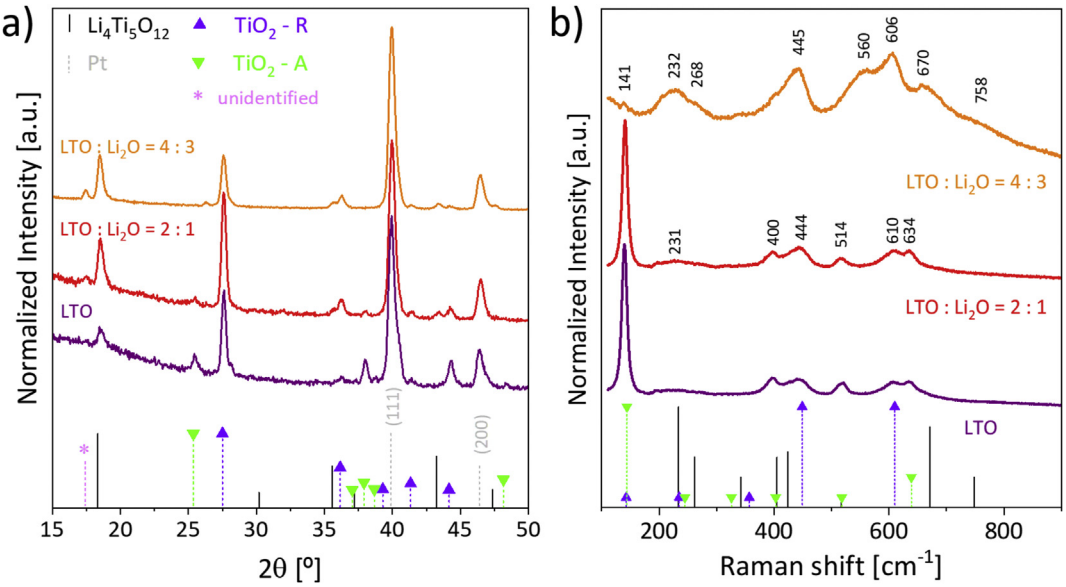

Fig. 2. GI-XRD of LTO thin films with different amounts of additional Li_2O in (a) and their corresponding Raman spectra in (b). Thin-film growth conditions are indicated with the deposition pulse ratio LTO:Li_2O (pulses on $Li_4Ti_5O_{12}$:pulses on Li_2O, respectively). X-ray patterns are referenced to the JCPDS database for $Li_4Ti_5O_{12}$ (00-049-0207), TiO_2-rutile (01-078-1510), TiO_2-anatase (01-073-1764), and Pt (01-087-0640) as substrates. An additional phase (pink asterisk) could not be assigned to a specific material pattern with certainty. Raman references are deduced from the literature [8].

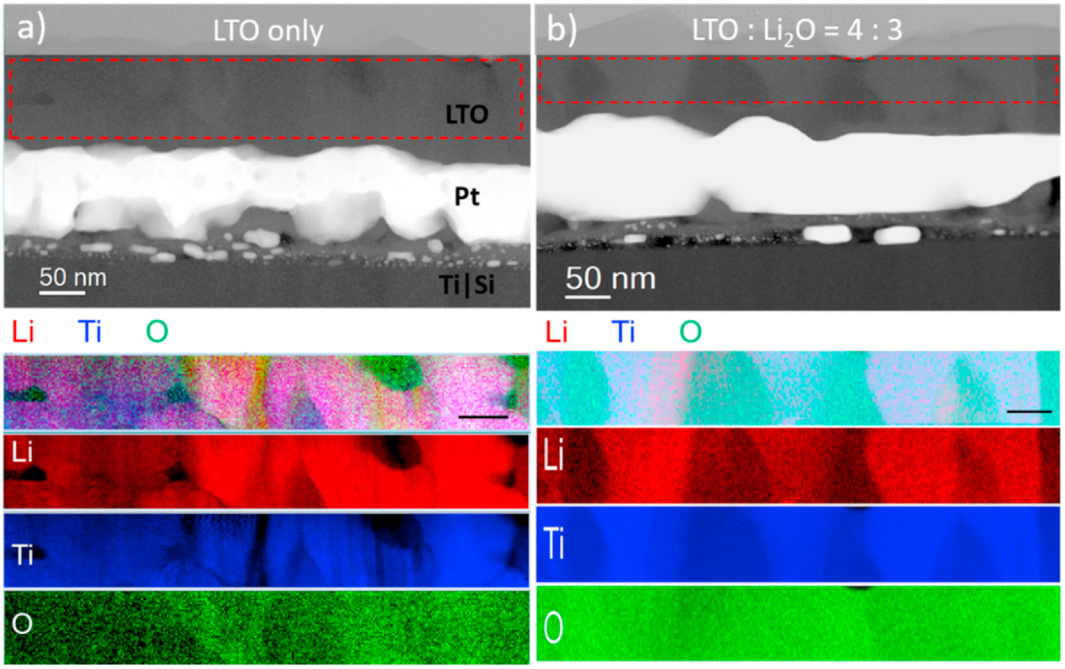

Fig. 3. STEM-HAADF images of LTO in (a) and LTO:Li_2O with 4:3 in (b) are shown. Corresponding STEM-EELS analysis for the region of interest (surrounded with red dashed lines) is shown below for each of the samples. The elemental maps of Li, Ti, and O are color-coded as red, blue, and green, respectively. The corresponding EELS spectra and further analyses are described in Section I in the Supporting Information.

correlated to a homogeneous distribution of oxygen. On the contrary, areas poor in Li and Ti have no impact on the strength in the oxygen signal, which remains congruent with its surrounding intensity. Compared to the LTO:Li_2O multilayer in Fig. 3(b), the elemental maps demonstrate better homogenization of the elemental distribution with a strong correlation between Ti and O signals. Especially, the lithium signal indicates a noteworthy contrast between Li-rich and Li-poor areas.

As a result of the inhomogeneous Li distribution, a summed elemental map in Fig. 3(b) is highlighting the co-existence of Li-poor and Li-rich areas, assigned to titania nano-grains with LTO crystallites in a dense film, respectively. This supports previous conclusions from the GI-XRD and Raman spectroscopy in Fig. 2. Overall, the manufacturing approach exemplified here allows increasing the Li content on the film while tuning the landscape of secondary phases.

3.2. Electrochemical performance of the films

The electrochemical performance of all thin films has been evaluated in 1 M $LiPF_6$ electrolyte with EC/DMC of 1:1 and lithium acting as counter and reference electrodes in a classic three-electrode setup. The thin films are assumed to be fully dense with $\rho = 3.62$ g/cm^3, which is supported by SEM images in Fig. 1, and the theoretical capacity for $Li_7Ti_5O_{12}$ is known to be 175 mAh/g when exchanging three lithium ions [15]. Cyclic voltammograms reveal different electrochemical reactions taking place in Fig. 4. The standard reaction potential for the intercalation of three Li^+ into spinel $Li_4Ti_5O_{12}$ is known to be 1.5 V vs. Li/Li$^+$ and follows the mechanism expressed in Eq. S1. Under continued discharge below 0.6 V vs. Li/Li$^+$, two additional lithium ions can be intercalated at tetrahedral 8a sites in $Li_7Ti_5O_{12}$ by reducing two remaining Ti^{4+} as described in Eq. S2, leading to a theoretical capacity of 239 mAh/g for $Li_9Ti_5O_{12}$ [46]. Most applications restrict to the limited potential window above 1.0 V vs. Li/Li$^+$ as the theoretical acceptance of Li^+ was believed to solely depend on the presence of vacant octahedral sites, potentially unavailable below 1.0 V [14,47]. On the contrary, current investigations by Yi et al. [16] and other groups [48] have proven the capability of $Li_7Ti_5O_{12}$ in hosting two additional Li^+ at vacant tetrahedral 8a sites in its lattice when operating at potentials as low as 0.01 V vs. Li/Li$^+$.

Cyclic voltammograms (CVs) and chronopotentiometry measurements have been collected at different current densities in the potential range of 0.3–3.5 V vs. Li/Li$^+$ and are shown in Fig. 4 for LTO layers of ablation ratios with 1:0 (a and b), 2:1 (c and d), and 4:3

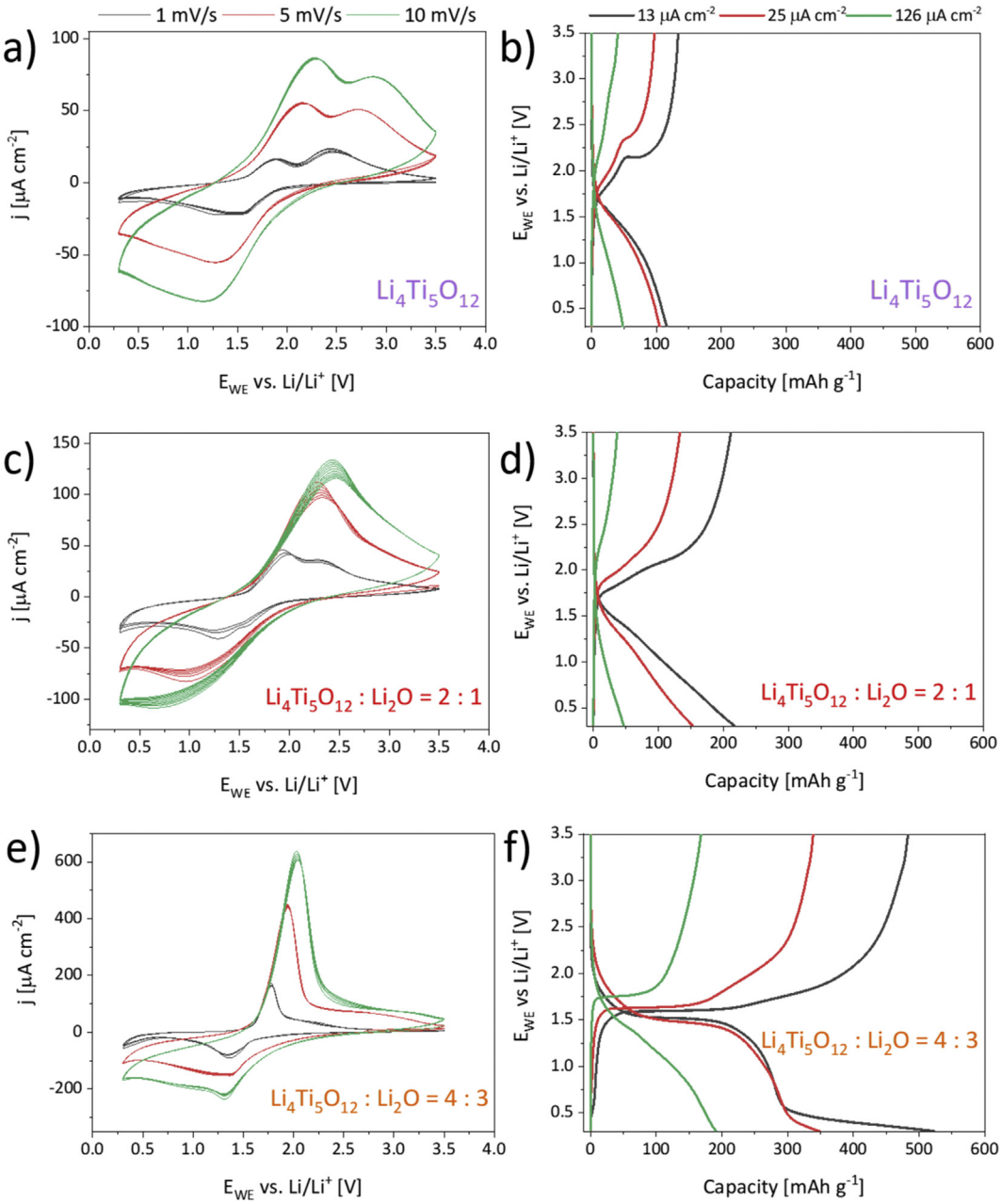

Fig. 4. Cyclic voltammograms (left) and constant current charge/discharge curves (right) of LTO layers without additional Li_2O in (a and b) and with additional Li_2O in a pulse ratio of 2:1 (c and d) and 4:3 (e and f) for LTO:Li_2O, respectively. The electrochemical window ranges between 0.3 and 3.5 V vs. Li/Li$^+$. The applied current densities are 13 µA/cm^2, 25 µA/cm^2, and 126 µA/cm^2.

(e and f) of LTO:Li_2O, respectively. For the calculation of specific capacities, the thicknesses determined by SE in Table S1 (see Supporting Information) were used.

A clear improvement in the mass transport kinetics and specific capacities can be observed in Fig. 4 when Li_2O has been introduced in the PLD process, especially concerning the total charge attained in the LTO lattice under fast cycling. The reversible redox peaks ascribed to $Ti^{3+/4+}$ are visible for all thin films in the CVs around 1.5 V and lower for anodic currents (discharge), as well as around 2.0 V and higher for cathodic currents (charge). Potential shifts depend on the applied scan rate and therefore different over-potentials. An additional oxidation peak is present for layers of lower lithium content in Fig. 4(a and c) at a potential of ~2.5 V vs. Li/Li^+, which in comparison to the literature may be attributed to different local coordination of titanium atoms or nanoshapes in the lattice [5,7,49]. Subsequent cycling proved the stability of the appearing oxidation and reduction peaks during charge and discharge, concluding full reversibility of the redox processes.

Constant current charge and discharge (chronopotentiometry) curves in Fig. 4(b, d, and f) exhibit a steady increase in the specific capacities, strongly correlated to the addition of Li_2O during deposition. For very low current densities of 13 μA/cm^2, the specific capacity nearly doubles for each time more Li_2O is added during deposition. The broad electrochemical window of 0.3–3.5 V vs. Li/Li^+ allows the lithiation of $Li_{7+x}Ti_5O_{12}$, with a theoretical capacity of 239 mAh/g for $x \approx 2$, which is first approximated by compositions of 2:1 with 221 mAh/g discharge capacity. Excellent charge/discharge profiles are reached with well-defined plateaus for the $Ti^{3+/4+}$ transition (Fig. 4(f)) under further Li_2O addition, resulting in an extraordinary high specific discharge capacity of 298 mAh/g at 0.5 V vs. Li/Li^+ for the 4:3 ablation ratio. An additional plateau appears to begin below 0.5 V vs. Li/Li^+, which may be attributed to the extra lithium uptake described earlier by Yi et al. [16] under the occupation of octahedral 16c and tetrahedral 8a sites [48]. The calculated gravimetric specific capacities are extracted at 0.5 V vs. Li/Li^+ for all thin films in Fig. 5 and plotted over their corresponding C-rates. Theoretical specific capacities C_{th} of $Li_7Ti_5O_{12}$ and $Li_9Ti_5O_{12}$ are indicated by the horizontal dashed lines at 175 mAh/g (gray) and 293 mAh/g (red) [23,48].

The values of C_{th} are approximated when LTO thin films of low additional Li content (1:0 and 2:1) are discharged at current densities between 13 and 25 μA/cm^2 (equal to C-rates below 4 C). A higher lithium content (4:3) is providing for the same current densities much lower C-rates and exceeds the theoretical capacity of $Li_9Ti_5O_{12}$ already at 0.5 V vs. Li/Li^+ by 30% at 0.5 C. With a higher current density, where films of less additional lithium visibly tend to fail meeting the desired capacitive values, LTO with the highest lithium content still retains the theoretical capacity of $Li_7Ti_5O_{12}$ with 175 mAh/g at 0.5 V, for a C-rate of 14 C in a potential window of 0.3–3.5 V vs. Li/Li^+. These capacities, higher than the usually reported values for bulk LTO, are in good agreement with the electrochemical behavior demonstrated on titanium-based nanosized particles [4,5,7,50]. In addition, the apparent charge storage could be maximized when discharging down to 0.01 V vs. Li/Li^+. This, however, depends on the film stability and the formation of a stable SEI, usually considered as responsible for a large capacitive drop in the first electrochemical cycles [7].

To prove cycling stability as a function of the cut-off voltage in films with high Li content, charge/discharge curves have been repeated and the capacity is extracted over 10 cycles per cut-off voltage at current densities of 20–30 μA/cm^2 (0.8–5.2 C-rate, Fig. 6). Stable capacity values are obtained for cut-off voltages ranging from 1.0 to 0.2 V vs. Li/Li^+. At this lower cut-off voltage, capacities around 230 mAh/g are reversibly extracted between $Li_4Ti_5O_{12}$ and $Li_{8.5}Ti_5O_{12}$ compositions, in accordance with experimental [48] and theoretical [51] reports. These stable high capacities remark the ability of our films to have lithium inserted beyond the usual $Li_7Ti_5O_{12}$ and extend the useful cycling range of LTO anodes. A certain stabilization of the capacity occurs at a cut-off voltage of 0.4 V, probably due to the incipient formation of $Li_{7+x}Ti_5O_{12}$ phases. We argue that a pseudocapacitive contribution to the capacity is not likely, given the low roughness of our films and the continuous increase in capacity with decreasing cut-off voltage during cycling. We suspect that such high capacities arise as a consequence of the extra Li-insertion in the nanocomposite LTO–TiO_2 structure of our films. Very similar electrochemical behavior and capacity values have been demonstrated for nanosheet composites [40]. In addition, grain boundaries between the two phases can play a key role in enhancing Li-diffusion into the bulk of the grains due to the generation of more fast-conducting interfacial domains [15,18]. This stability, however, is quickly lost as the cut-off voltage is further decreased to 0.01 V. The capacity decay even persists when the cut-off voltage is increased again to 1.0 V, evidencing a progressive increase of the polarization after being cycled at very low potentials and fast rates.

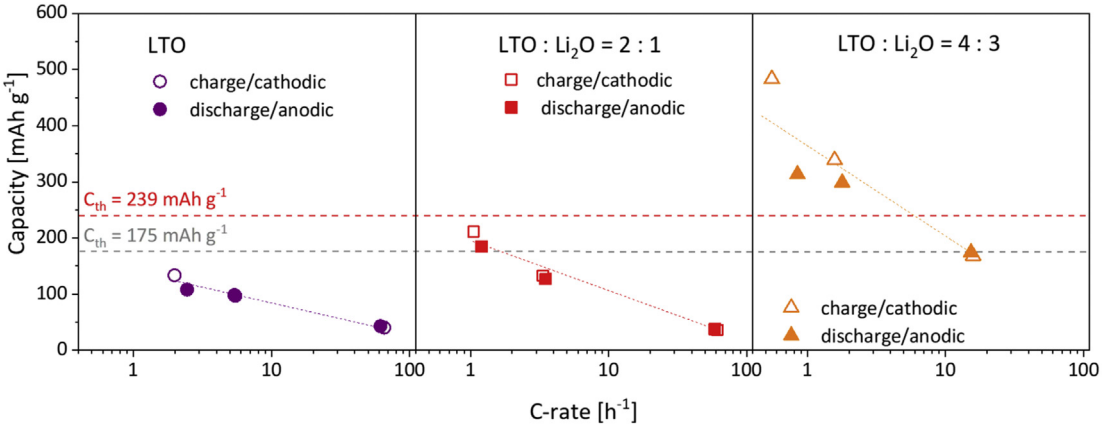

Fig. 5. Capacitive values taken at 3.5 V for charge curves (empty symbols) and at 0.5 V vs. Li/Li^+ for discharge curves (filled symbols) of LTO multilayers at different C-rates (logarithmic scale) for pulse ratios of 1:0 (circles), 2:1 (squares), and 4:3 (triangles) of LTO:Li_2O during PLD depositions, respectively. The theoretical specific capacities for LTO are indicated by horizontal dashed lines corresponding to 175 mAh/g (gray) and 293 mAh/g (red) [23,48]. The applied current densities are ascending with the C-rates and correspond to 13 μA/cm^2, 25 μA/cm^2, and 126 μA/cm^2 for all samples.

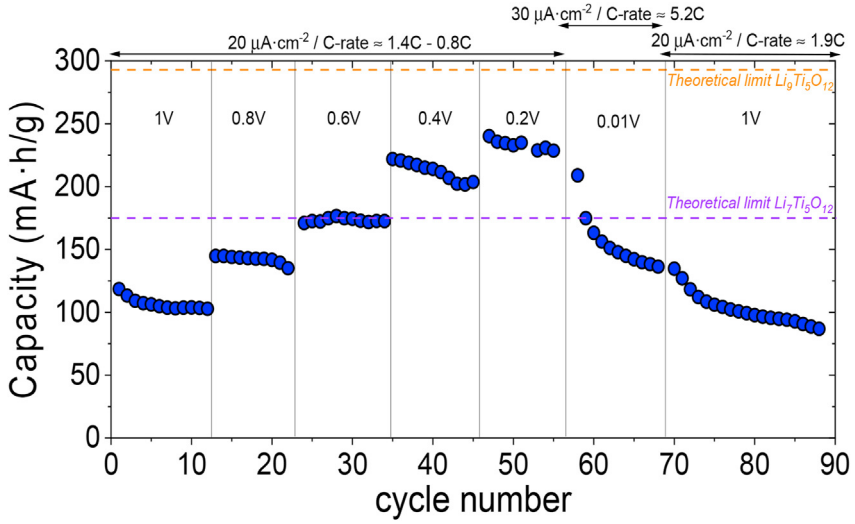

Fig. 6. Extracted capacities from charge/discharge curves at a constant current density of 20 μA/cm^2 at different cut-off voltages. For the cycles at 0.01 V, a 30 μA/cm^2 current density was employed.

3.3. Operando characterization of the discharge to very low potentials

To obtain further insights into the (micro)structural evolution of the thin films when discharging to very low potentials, we performed *operando* SE during the first cycle on a pristine film with high Li content (LTO:Li_2O ratio of 4:3) and an ex-situ Raman analysis before and after the electrochemical measurements. Let us first state that a detailed SE study of the optical properties dependency on the addition of Li_2O preceded the following analysis (see Supporting Information, Section III).

As previously mentioned, for this *operando* analysis, we employed a low discharge current (3.5 μA/cm^2, 0.17 C-rate) to shed some light on the kinetics of the SEI formation and/or degradation mechanisms. The inset of Fig. 7a (and Fig. S7 in the Supporting Information) shows the first constant current charge−discharge curves collected for these conditions. The very first cycle shows the expected electrochemical features of the Li-insertion in the films, reaching a capacity value of 470 mAh/g at 0.01 V. However, the following charge cycle only reaches a capacity of 121 mAh/ g, which keeps decreasing in subsequent cycles. Such a large decrease is not observed when the films are cycled at higher C-rates (Fig. 6), suggesting a kinetic-limited degradation mechanism at low potentials. Similar observations in LTO−TiO_2 composites were previously attributed to changes in the titania secondary phases [37].

The first output of our SE analysis is the thickness evolution of the lithiated layer with time for the three different regimes (open symbols in Fig. 7a referred to the right y-axis). Remarkably, the thickness evolution of the entire film follows quite accurately the shape of the charge injection for regimes I ($\Delta t \sim -2.5 \pm 2$ nm), II ($\Delta t \sim -2.9 \pm 2$ nm more), and III ($\Delta t \sim 1.51 \pm 2$ nm), which indicates a change in volume upon lithiation/delithiation. Despite this good correlation, the thickness of the layer does not recover the initial values after charging in regime III (but the ones obtained at the beginning of regime II). In the imaginary part of the dielectric function (ε_i), two distinctive features evolving with time are present in all cases, namely, a lower band (in the next "low energy mode", assigned to O (2p)−Ti (3d) state transition [52]) at ~1.5 eV and a higher band (in the next "high energy mode", assigned to $Ti^{3+/4+}$ (t_{2g}−e_g)) at ~4 eV (Fig. 7b). A detailed evolution with time of two descriptors of the optical properties, i.e. the frequency and amplitude of these two bands are presented in Fig. 7c and d, respectively. For regime I, the amplitude of the high energy band decreases while the low energy absorption increases. For regimes II and III, both modes increase and decrease together, respectively.

For regime I, our data are in excellent agreement with previous experimental results and first-principle calculations [52,53]. Beyond $Li_7Ti_5O_{12}$, i.e. regime II, the lithiation process is far less explored and, to the best of our knowledge, there is no experimental data to compare with. Despite the lack of measurements, ab-initio studies suggest that the high energy mode could be shifted toward higher energies (wider band gap) while increasing the availability of electronic states at the low, intermediate, and high energy regions [51]. This shifting is observed in our experimental data (see Fig. 7b). Regarding the observed increase in intensity for both energy modes, they can also be related to the role of oxygen in this regime upon further lithium insertion, which has been shown to produce either a displacement of the O atoms [50,51] or a charge compensation occurring at the O sites for nano-sized samples [54]. An eventual oxygen displacement could create extra available electronic states [54] while the presence (and/or generation) of oxygen vacancies could generate further available mid-gap states at low energies through small polaron formation [55−57].

Finally, during the charging process (regime III), both energy modes decrease their intensity (Fig. 7b) recovering the values of regime II, but not those of regime I, which now seem to be blocked. In terms of Li occupation, these observations indicate that only the Li inserted in regime II (at the 8a tetrahedral sites) was extracted upon charging, while the Li inserted in regime I (at 16c positions) could not leave the structure, despite the low charging current employed. This discards the scenario in which Li^+ is not inserted at low potentials (at the expense of extracting oxygen), given that the capacity generated at low potentials is the one that is being electrochemically recovered.

Overall, our results back up the relevant idea that the cycling range of LTO-based systems can be safely extended until the limit of ~0.2 V, which is beyond the typical value of 1 V reported in the literature. Beyond that point, Li-insertion can lead to a large simultaneous occupation of tetrahedral and octahedral positions and a concurrent suppression of ionic diffusion [23,50], effectively restraining the migration of Li-ions anchored at 16c positions.

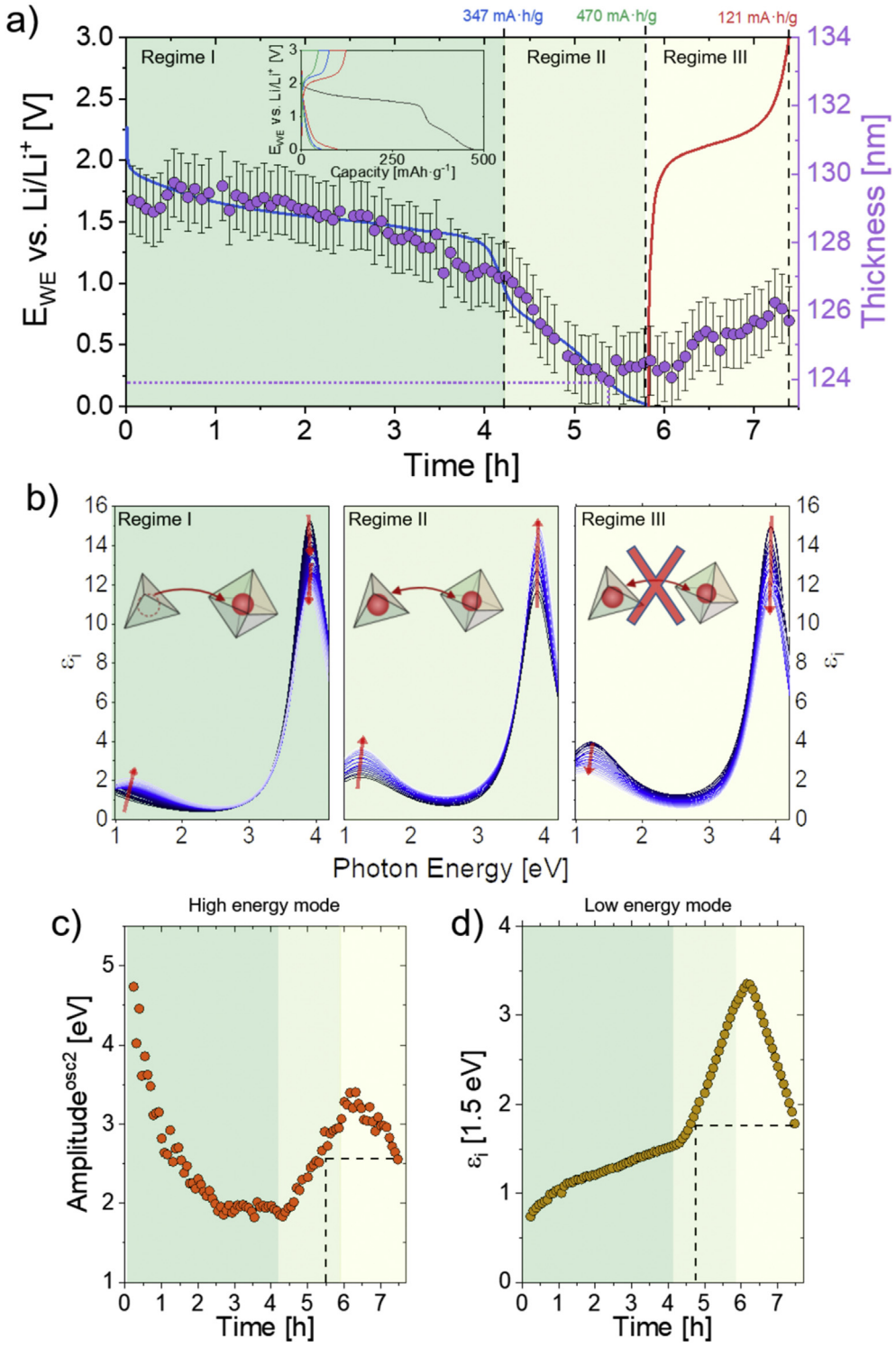

Fig. 7. (a) Constant current charge and discharge curves collected under a current density of 3.6 μA/cm^2 (0.17 C-rate) monitored by *operando* SE with an acquisition rate of ~4 min/spectrum. The inset shows the charge/discharge profiles of the *operando* experiment as a function of capacity (see Fig. S7 in the Supporting Information for an enlarged version of the image). The right-axis (purple) shows the thickness evolution of the entire film with time (error bars are ±1 nm). (b) Optical absorption as a function of the photon energy corresponding to the three different regimes (arrows indicate the evolution with time along the experiment). Insets represent the lithium occupancy in the LTO lattice. (c) Time evolution of the amplitude of the oscillator of the high energy mode. (d) Time evolution of the optical absorption at 1.5 eV.

3.4. Postmortem Raman spectroscopy analysis

To understand microstructural changes occurring during extended-range cycling, Raman spectroscopy was performed before and after (Fig. 8, section IV in the Supporting Information). All vibrational modes, including those of rutile, are shifted toward larger wavelength numbers (blue shift, shorter bond lengths after cycling) while no new peaks are detected in the

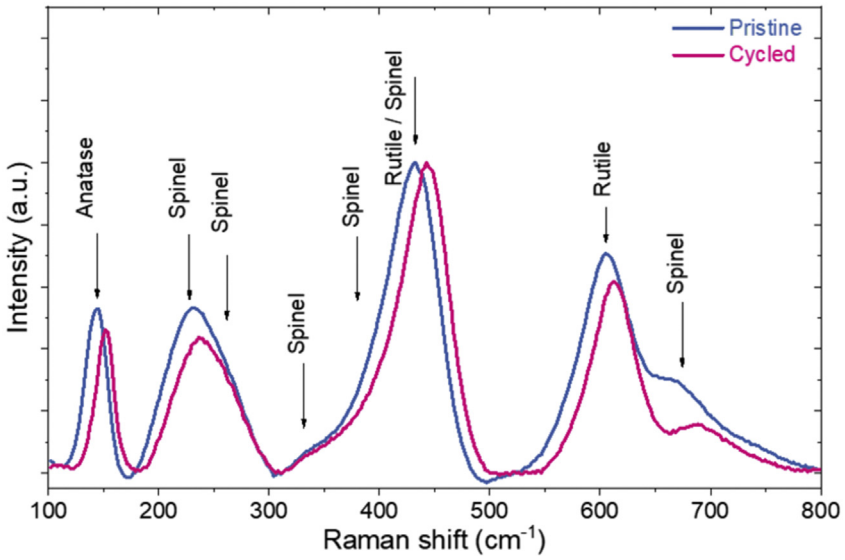

Fig. 8. Raman spectroscopy performed before and after the electrochemical measurements.

spectrum. The largest change appears in the A_{1g} mode of the spinel at 671/cm, which shifts at 690/cm after operation. Remarkably, similar blueshifts have been reported for oxygen-deficient LTO [58] and anatase [59] phases, in contrast to the expected redshift in the Raman peaks for stoichiometric $Li_7Ti_5O_{12}$ [28,60]. This resemblance to reported oxygen-deficient LTO makes us wonder whether oxygen vacancies are generated as a consequence of the imposed electric field and side reactions with the electrolyte. In the same direction, distortions toward shorter bond lengths in the oxygen environment are expected at lithiation degrees beyond $Li_7Ti_5O_{12}$. Interestingly, the rutile A_{1g} mode blue shifts from 605/cm in the pristine state – expressing the presence of oxygen vacancies initially in rutile [61] – 611/cm after cycling – the canonical value of the rutile A_{1g} mode. This suggests that either Li^+ is inserted in rutile (although shifts from 612/cm to 625/cm are expected [62] and our films are not highly oriented along the (001) fast diffusion channel) or there is oxygen exchange between the LTO and the oxygen-deficient rutile grains at high Li^+ insertion. All in all, both scenarios (oxygen uptake/exchange vs. oxygen environment distortions) are compatible with the observed electrochemical behavior since they have an identical impact on the electrochemistry, i.e. the trapping of Li-ions at the 16c sites due to the rupture of ionic pathways. Finally, it is important to remark that the observed blue shifting in the Raman spectra involves a compression across the entire volume of the film, which is not compatible with having a thin SEI layer as the sole responsibility of the capacity loss or a pseudocapacitive storage mechanism. Further studies are needed to elucidate the exact nature of the Raman shifts and the role of rutile in the performance.

4. Conclusion

The alternating ablation of LTO and Li_2O targets in the PLD provides a good strategy to fabricate highly performing anodes, which sufficiently compensates for the loss of volatile elements during deposition. Maximum capacities were obtained for layers with a 4:3 (LTO:Li_2O) pulse ratio, leading to an exceptionally high specific discharge capacity of 298 mAh/ g at 0.5 V vs. Li/Li^+, for 0.5 C in the potential window of 0.3–3.5 V vs. Li/Li^+. Stable cycling was achieved down to potentials of 0.2 V, with a capacity of 230 mAh/g at 1.4 C. The structural consequences of cycling in the low potential region (down to 0.01 V vs. Li/Li^+) during the first discharge were studied using *operando* SE and ex-situ Raman spectroscopy. We provide evidence suggesting that a kinetically limited degradation mechanism occurs when cycling in the range of 0.2–0.01 V, which tends to trap Li-ions at the octahedral 16c positions. In pragmatic terms, we provide guidelines to extend the useful cycling range of LTO-based anodes to increase their competitiveness vs. Li-metal anodes.

CRediT author statement

Valerie Siller: Investigation, Writing - Original Draft, Writing - Review & Editing. **Juan Carlos Gonzalez-Rosillo**: Investigation, Writing - Original Draft, Writing - Review & Editing. **Marc Nuñez Eroles**: Methodology, Resources, Writing - Review & Editing. **Michel Stchakovsky**: Methodology, Investigation. **Raul Arenal**: Investigation, Writing - Review & Editing. **Alex Morata**: Supervision, Conceptualization, Writing - Review & Editing, Methodology. **Albert Tarancón**: Supervision, Conceptualization, Writing - Review & Editing, Funding acquisition.

Declaration of competing interest

The authors declare that they have no known competing financial interests or personal relationships that could have appeared to influence the work reported in this paper.

Acknowledgments

This project has received funding from the European Union's Horizon 2020 research and innovation program under grant agreement No 824072 (HARVESTORE), the European Regional Development Fund under the FEDER Catalonia Operative Programme 2014–2020 (FEM-IoT, 001-P-00166), and the "Generalitat de Catalunya" (2017 SGR 1421, NANOEN). FIB, STEM, and STEM-EELS studies were conducted at the Laboratorio de Microscopias Avanzadas, Universidad de Zaragoza, Spain. R. A. gratefully acknowledges the support from the Spanish MICINN through project grant PID2019-104739 GB-100/AEI/10.13039/501100011033, from the Government of Aragon (project DGA E13-20R) and European Union H2020 program "ESTEEM3" (823717). J.

C. G.- R., acknowledges the financial support provided by the European Union's Horizon 2020 research and innovation program under the Marie Skłodowska-Curie Grant Agreement No. 801342 (Tecniospring INDUSTRY), as well as by the Agency for Business Competitiveness of the Government of Catalonia. Spectroscopic Ellipsometry measurements and models have been developed in collaboration with HORIBA France SAS. Suitable Pt-covered Si substrates have been provided by the Institute of Microelectronics of Barcelona IMB-CNM. GI-XRD measurements have been collected at the Scientific and Technological Center (CCiT) at the University of Barcelona.

Appendix A. Supplementary data

Supplementary data to this article can be found online at https://doi.org/10.1016/j.mtener.2022.100979.

References

[1] M. Pasta, D. Armstrong, Z.L. Brown, J. Bu, M.R. Castell, P. Chen, A. Cocks, S.A. Corr, E.J. Cussen, E. Darnbrough, V. Deshpande, C. Doerrer, M.S. Dyer, H. El-Shinawi, N. Fleck, P. Grant, G.L. Gregory, C. Grovenor, L.J. Hardwick, J.T.S. Irvine, H.J. Lee, G. Li, E. Liberti, I. McClelland, C. Monroe, P.D. Nellist, P.R. Shearing, E. Shoko, W. Song, D.S. Jolly, C.I. Thomas, S.J. Turrell, M. Vestli, C.K. Williams, Y. Zhou, P.G. Bruce, 2020 roadmap on solid-state batteries, J. Phys. Energy 2 (2020) 032008, https://doi.org/10.1088/2515-7655/ab95f4.

[2] K. Rose, S. Eldridge, L. Chapin, The internet OF things: AN overview. Understanding the issues and challenges of a more connected world, Internet Soc. (2015) 80.

[3] A. Mukanova, A. Jetybayeva, S.T. Myung, S.S. Kim, Z. Bakenov, A mini-review on the development of Si-based thin film anodes for Li-ion batteries, Mater. Today Energy 9 (2018) 49–66, https://doi.org/10.1016/j.mtener.2018.05.004.

[4] S. Bach, J.P. Pereira-Ramos, P. Willman, Investigation of lithium diffusion in nano-sized rutile TiO 2 by impedance spectroscopy, Electrochim. Acta 55 (2010) 4952–4959, https://doi.org/10.1016/j.electacta.2010.03.101.

[5] V. Subramanian, A. Karki, K.I. Gnanasekar, F. Posey, B. Rambabu, Nanocrystalline TiO 2 (anatase) for Li-ion batteries, J. Power Sources 159 (2006) 186–192, https://doi.org/10.1016/j.jpowsour.2006.04.027.

[6] M. Wagemaker, W.J.H. Borghols, F.M. Mulder, Large impact of particle size on insertion reactions. A Case for Anatase Li x TiO 2, 2007, pp. 4323–4327, 11.

[7] S.B. Patil, H. Phattepur, B. Kishore, R.V.G. Nagaraju, Robust electrochemistry of black - TiO 2 as stable and high - rate negative electrode for lithium-ion batteries, Mater. Renew. Sustain. Energy 8 (2019) 1–10, https://doi.org/10.1007/s40243-019-0147-y.

[8] A. Lakshmi-Narayana, O.M. Hussain, A. Mauger, C. Julien, Transport properties of nanostructured Li2 Ti O_3 anode material synthesized by hydrothermal method, Science 1 (2019) 1–16.

[9] T. Ogihara, T. Kodera, Synthesis of Li 2 Ti 3 O 7 anode materials by ultrasonic spray pyrolysis and their electrochemical properties, Materials (Basel) (2013) 2285–2294, https://doi.org/10.3390/ma6062285.

[10] G. Xu, P. Han, S. Dong, H. Liu, G. Cui, L. Chen, Li4Ti5O12-based energy conversion and storage systems: status and prospects, Coord. Chem. Rev. 343 (2017) 139–184, https://doi.org/10.1016/j.ccr.2017.05.006.

[11] A.K. Haridas, C.S. Sharma, N.Y. Hebalkar, T.N. Rao, Nano-grained SnO2/Li4Ti5O12 composite hollow fibers via sol-gel/electrospinning as anode material for Li-ion batteries, Mater. Today Energy 4 (2017) 14–24, https://doi.org/10.1016/j.mtener.2017.01.002.

[12] J.-T. Han, Y.-H. Huang, J.B. Goodenough, New anode framework for rechargeable lithium batteries, Chem. Mater. 23 (2011) 2027–2029.

[13] D. Liu, C. Ouyang, J. Shu, J. Jiang, Z. Wang, L. Chen, Theoretical study of cation doping effect on the electronic conductivity of Li 4 Ti 5 O 12, Phys. Status Solidi 1841 (2006) 1835–1841, https://doi.org/10.1002/pssb.200541404.

[14] J. Deng, Z. Lu, C.Y. Chung, X. Han, Z. Wang, Electrochemical performance and kinetic behavior of lithium-ion in Li 4 Ti 5 O 12 thin-film electrodes, Appl. Surf. Sci. 314 (2014) 936–941, https://doi.org/10.1016/j.apsusc.2014.06.162.

[15] D.M. Cunha, T.A. Hendriks, A. Vasileiadis, C.M. Vos, T. Verhallen, D.P. Singh, M. Wagemaker, M. Huijben, Doubling reversible capacities in epitaxial Li4 Ti5 O12 thin film anodes for microbatteries, ACS Appl. Energy Mater. 2 (2019) 3410–3418, https://doi.org/10.1021/acsaem.9b00217.

[16] T.-F. Yi, S.-Y. Yang, Y. Xie, Recent advances of Li4 Ti5 O12 as promising next generation anode material for high power lithium-ion batteries, J. Mater. Chem. A. 3 (2015) 5750–5777, https://doi.org/10.1039/C4TA06882C.

[17] Y. Cai, Y. Huang, W. Jia, X. Wang, Y. Guo, D. Jia, Z. Sun, W. Pang, Z. Guo, Super high-rate, long cycle life of europium modified carbon coated hierarchical mesoporous lithium titanate anode materials for lithium ion batteries, J. Mater. Chem. A. 4 (2016) 9949–9957, https://doi.org/10.1039/C6TA03162E.

[18] W. Zhang, D. Seo, T. Chen, L. Wu, M. Topsakal, Y. Zhu, D. Lu, G. Ceder, F. Wang, Kinetic pathways of ionic transport in fast-charging lithium titanate, Science 367 (2020) 1030–1034, https://doi.org/10.1126/science.aax3520, 80.

[19] S. Ganapathy, A. Vasileiadis, J.R. Heringa, M. Wagemaker, The fine line between a two-phase and solid-solution phase transformation and highly mobile phase interfaces in spinel Li 4+ x Ti 5 O 12, Adv. Energy Mater. 7 (2017) 1601781, https://doi.org/10.1002/aenm.201601781.

[20] C.Y. Ouyang, Z.Y. Zhong, M.S. Lei, Ab initio studies of structural and electronic properties of Li4Ti5O12 spinel, Electrochem. Commun. 9 (2007) 1107–1112, https://doi.org/10.1016/j.elecom.2007.01.013.

[21] P. Jakes, J. Granwehr, H. Kungl, R.-A. Eichel, Mixed ionic-electronic conducting Li4 Ti5 O12 as anode material for lithium ion batteries with enhanced rate capability - impact of oxygen non-stoichiometry and aliovalent Mg2+-doping studied by electron paramagnetic resonance, Z. Phys. Chem. 229 (2015), https://doi.org/10.1515/zpch-2015-0618.

[22] J.P. Pender, G. Jha, D.H. Youn, J.M. Ziegler, I. Andoni, E.J. Choi, A. Heller, B.S. Dunn, P.S. Weiss, R.M. Penner, C.B. Mullins, Electrode degradation in lithium-ion batteries, ACS Nano 14 (2020) 1243–1295, https://doi.org/10.1021/acsnano.9b04365.

[23] C. Han, Y.B. He, S. Wang, C. Wang, H. Du, X. Qin, Z. Lin, B. Li, F. Kang, Large polarization of Li4Ti5O12 lithiated to 0 v at large charge/discharge rates, ACS Appl. Mater. Interfaces 8 (2016) 18788–18796, https://doi.org/10.1021/acsami.6b04239.

[24] S. Lobe, A. Bauer, S. Uhlenbruck, D. Fattakhova-Rohlfing, Physical vapor deposition in solid state battery development: from materials to devices, Adv. Sci. (2021) 2002044, https://doi.org/10.1002/advs.202002044, 2002044.

[25] F. Pagani, M. Döbeli, C. Battaglia, Lithium-ion transport in Li 4 Ti 5 O 12 epitaxial thin films vs. State of charge, Batter. Supercaps. 4 (2021) 316–321, https://doi.org/10.1002/batt.202000159.

[26] J. Speulmanns, A.M. Kia, S. Bönhardt, W. Weinreich, P. Adelhelm, Atomic layer deposition of textured Li4Ti5O12: a high-power and long-cycle life anode for lithium-ion thin-film batteries, Small 17 (2021), https://doi.org/10.1002/smll.202102635.

[27] F. Pagani, E. Stilp, R. Pfenninger, E.C. Reyes, A. Remhof, Z. Balogh-Michels, A. Neels, J. Sastre-Pellicer, M. Stiefel, M. Döbeli, M.D. Rossell, R. Erni, J.L.M. Rupp, C. Battaglia, Epitaxial thin films as a model system for Li-ion conductivity in Li 4 Ti 5 O 12, ACS Appl. Mater. Interfaces 10 (2018) 44494–44500, https://doi.org/10.1021/acsami.8b16519.

[28] J.C. Gonzalez-Rosillo, M. Balaish, Z.D. Hood, N. Nadkarni, D. Fraggedakis, K.J. Kim, K.M. Mullin, R. Pfenninger, M.Z. Bazant, J.L.M. Rupp, Lithium-battery anode gains additional functionality for neuromorphic computing through metal–insulator phase separation, Adv. Mater. 32 (2020) 1907465, https://doi.org/10.1002/adma.201907465.

[29] M. Balaish, J.C. Gonzalez-Rosillo, K.J. Kim, Y. Zhu, Z.D. Hood, J.L.M.M. Rupp, Processing thin but robust electrolytes for solid-state batteries, Nat. Energy 6 (2021) 227–239, https://doi.org/10.1038/s41560-020-00759-5.

[30] Y. Zhu, J.C. Gonzalez-Rosillo, M. Balaish, Z.D. Hood, K.J. Kim, J.L.M. Rupp, Lithium-film ceramics for solid-state lithionic devices, Nat. Rev. Mater. 6 (2021) 313–331, https://doi.org/10.1038/s41578-020-00261-0.

[31] M. Fehse, R. Trócoli, E. Hernández, E. Ventosa, A. Sepúlveda, A. Morata, A. Tarancón, An innovative multi-layer pulsed laser deposition approach for LiMn2O4 thin film cathodes, Thin Solid Films 648 (2018) 108–112, https://doi.org/10.1016/j.tsf.2018.01.015.

[32] M. Fehse, R. Trócoli, E. Ventosa, E. Hernández, A. Sepúlveda, A. Morata, A. Tarancón, Ultrafast dischargeable LiMn 2 O 4 thin-film electrodes with pseudocapacitive properties for microbatteries, ACS Appl. Mater. Interfaces 9 (2017) 5295–5301, https://doi.org/10.1021/acsami.6b15258.

[33] J. Huang, W. Li, H. Yang, J.L. MacManus-Driscoll, Tailoring physical functionalities of complex oxides by vertically aligned nanocomposite thin-film design, MRS Bull. 46 (2021) 159–167, https://doi.org/10.1557/s43577-021-00028-0.

[34] F. Baiutti, F. Chiabrera, M. Acosta, D. Diercks, D. Parfitt, J. Santiso, X. Wang, A. Cavallaro, A. Morata, H. Wang, A. Chroneos, J. MacManus-Driscoll, A. Tarancon, A high-entropy manganite in an ordered nanocomposite for long-term application in solid oxide cells, Nat. Commun. 12 (2021) 2660, https://doi.org/10.1038/s41467-021-22916-4.

[35] D.M. Cunha, M. Huijben, Lithium-based vertically aligned nanocomposites for three-dimensional solid-state batteries, MRS Bull. 46 (2021) 152–158, https://doi.org/10.1557/s43577-021-00026-2.

[36] B. Zhao, R. Ran, M. Liu, Z. Shao, A comprehensive review of Li4Ti5O12-based electrodes for lithium-ion batteries: the latest advancements and future perspectives, Mater. Sci. Eng. R Rep. 98 (2015) 1–71, https://doi.org/10.1016/j.mser.2015.10.001.

[37] L. Yang, H. Li, J. Liu, Y. Lu, S. Li, J. Min, N. Yan, Z. Men, M. Lei, Effects of TiO2 phase on the performance of Li4Ti5O12 anode for lithium-ion batteries, J. Alloys Compd. 689 (2016) 812–819, https://doi.org/10.1016/j.jallcom.2016.08.059.

[38] S. Pal, S. Roy, P. Jalagam, P. Basak, Nanostructured Li4Ti5O12Anodes: delineating the impact of morphology, exposed facets, and phase purity on the performance, ACS Appl. Energy Mater. 4 (2021) 969–984, https://doi.org/10.1021/acsaem.0c02929.

[39] T.F. Yi, Z.K. Fang, Y. Xie, Y.R. Zhu, S.Y. Yang, Rapid charge-discharge property of Li4Ti5O12-TiO2 nanosheet and nanotube composites as anode material for power lithium-ion batteries, ACS Appl. Mater. Interfaces 6 (2014) 20205–20213, https://doi.org/10.1021/am5057568.

[40] M. Ding, H. Liu, X. Zhao, L. Pang, L. Deng, M. Li, Composite with TiO2 and extension of discharge voltage range for capacity enhancement of a Li4Ti5O12 battery, RSC Adv. 7 (2017) 43894–43904, https://doi.org/10.1039/c7ra07390a.

[41] H.S. Bhatti, D.H. Anjum, S. Ullah, B. Ahmed, A. Habib, A. Karim, S.K. Hasanain, Electrochemical characteristics and li+ ion intercalation kinetics of dual-phase li4ti5o12/li2tio3 composite in the voltage range 0-3 v, J. Phys. Chem. C 120 (2016) 9553–9561, https://doi.org/10.1021/acs.jpcc.5b12114.
[42] C. Jeanguillaume, C. Colliex, Spectrum-image: the next step in EELS digital acquisition and processing, Ultramicroscopy 28 (1989) 252–257, https://doi.org/10.1016/0304-3991(89)90304-5.
[43] R. Arenal, F. de la Peña, O. Stéphan, M. Walls, M. Tencé, A. Loiseau, C. Colliex, Extending the analysis of EELS spectrum-imaging data, from elemental to bond mapping in complex nanostructures, Ultramicroscopy 109 (2008) 32–38, https://doi.org/10.1016/j.ultramic.2008.07.005.
[44] S. Canulescu, E.L. Papadopoulou, D. Anglos, T. Lippert, C.W. Schneider, A. Wokaun, Mechanisms of the laser plume expansion during the ablation of LiMn 2O4, J. Appl. Phys. 105 (2009), https://doi.org/10.1063/1.3095687.
[45] H. Lindström, S. Södergren, A. Solbrand, H. Rensmo, J. Hjelm, A. Hagfeldt, S.-E. Lindquist, Li+ ion insertion in TiO 2 (anatase). 2. Voltammetry on nanoporous films, J. Phys. Chem. B 2 (1997) 7717–7722, https://doi.org/10.1021/jp970490q.
[46] M.W. Raja, S. Mahanty, M. Kundu, R.N. Basu, Synthesis of nanocrystalline Li 4 Ti 5 O 12 by a novel aqueous combustion technique, J. Alloys Compd. 468 (2009) 258–262, https://doi.org/10.1016/j.jallcom.2007.12.072.
[47] H. Ge, N. Li, D. Li, C. Dai, D. Wang, Study on the theoretical capacity of spinel lithium titanate induced by low-potential intercalation, J. Phys. Chem. C 113 (2009) 6324–6326.
[48] H. Liu, Z. Zhu, J. Huang, X. He, Y. Chen, R. Zhang, R. Lin, Y. Li, S. Yu, X. Xing, Q. Yan, X. Li, M.J. Frost, K. An, J. Feng, R. Kostecki, H. Xin, S.P. Ong, P. Liu, Elucidating the limit of Li insertion into the spinel Li4Ti5O12, ACS Mater. Lett. 1 (2019) 96–102, https://doi.org/10.1021/acsmaterialslett.9b00099.
[49] G. Wu, P. Li, C. Zhu, Y. Lei, H. Zhao, T. Li, H. Yue, B. Dou, Y. Gao, X. Yang, Amorphous titanium oxide passivated lithium titanium phosphate electrode for high stable aqueous lithium ion batteries with oxygen tolerance, Electrochim. Acta 246 (2017) 720–729, https://doi.org/10.1016/j.electacta.2017.06.093.
[50] W.J.H. Borghols, M. Wagemaker, U. Lafont, E.M. Kelder, F.M. Mulder, Size effects in the Li4+xTi5O12 spinel, J. Am. Chem. Soc. 131 (2009) 17786–17792, https://doi.org/10.1021/ja902423e.
[51] Z. Zhong, C. Ouyang, S. Shi, M. Lei, Ab initio studies on Li 4+ x Ti 5 O 12 compounds as anode materials for lithium-ion batteries, ChemPhysChem 9 (2008) 2104–2108, https://doi.org/10.1002/cphc.200800333.
[52] Y. Joshi, A. Saksena, E. Hadjixenophontos, J.M. Schneider, G. Schmitz, Electrochromic behavior and phase transformation in Li4+ xTi5O12 upon lithium-ion deintercalation/intercalation, ACS Appl. Mater. Interfaces 12 (2020) 10616–10625, https://doi.org/10.1021/acsami.9b19683.
[53] Y. Liu, J. Lian, Z. Sun, M. Zhao, Y. Shi, H. Song, The first-principles study for the novel optical properties of Li-Ti 2 O 4, Li 4 Ti 5 O 12, Li 2 Ti 2 O 4 and Li 7 Ti 5 O 12, Chem, Phys. Lett. 677 (2017) 114–119, https://doi.org/10.1016/j.cplett.2017.04.009.
[54] F. Wang, L. Wu, C. Ma, D. Su, Y. Zhu, J. Graetz, Excess lithium storage and charge compensation in nanoscale Li 4+ x Ti 5 O 12, Nanotechnology 24 (2013) 424006, https://doi.org/10.1088/0957-4484/24/42/424006.
[55] M. Kick, C. Scheurer, H. Oberhofer, Formation and stability of small polarons at the lithium-terminated Li 4 Ti 5 O 12 (LTO) (111) surface, J. Chem. Phys. 153 (2020) 144701, https://doi.org/10.1063/5.0021443.
[56] J. Qiu, C. Lai, E. Gray, S. Li, S. Qiu, E. Strounina, C. Sun, H. Zhao, S. Zhang, Blue hydrogenated lithium titanate as a high-rate anode material for lithium-ion batteries, J. Mater. Chem. A. 2 (2014) 6353–6358, https://doi.org/10.1039/c4ta00556b.
[57] J.H. Jeong, B.H. Park, G.W. Lee, K.C. Roh, K.B. Kim, Phase transformation of spinel Li4Ti5O12 to anatase TiO2 by catalytic delithiation, Energy Storage Mater. 25 (2020) 510–519, https://doi.org/10.1016/j.ensm.2019.09.031.
[58] Q. Xia, N. Jabeen, S.V. Savilov, S.M. Aldoshin, H. Xia, Black mesoporous Li4Ti5O12-δ nanowall arrays with improved rate performance as advanced 3D anodes for micro-batteries, J. Mater. Chem. A. 4 (2016) 17543–17551, https://doi.org/10.1039/c6ta06699b.
[59] G. Liu, H.G. Yang, X. Wang, L. Cheng, H. Lu, L. Wang, G.Q. Lu, H.M. Cheng, Enhanced photoactivity of oxygen-deficient anatase TiO2 sheets with dominant {001} facets, J. Phys. Chem. C 113 (2009) 21784–21788, https://doi.org/10.1021/jp907749r.
[60] C.M. Julien, M. Massot, K. Zaghib, Structural studies of Li4/3Me5/3O4(Me = Ti, Mn) electrode materials: local structure and electrochemical aspects, J. Power Sources 136 (2004) 72–79, https://doi.org/10.1016/j.jpowsour.2004.05.001.
[61] R.J. Betsch, H.L. Park, W.B. White, Raman spectra of stoichiometric and defect rutile, Mater. Res. Bull. 26 (1991) 613–622, https://doi.org/10.1016/0025-5408(91)90104-T.
[62] B. Pitna Laskova, L. Kavan, M. Zukalova, K. Mocek, O. Frank, In situ Raman spectroelectrochemistry as a useful tool for detection of TiO2(anatase) impurities in TiO2(B) and TiO2(rutile), Monat. Fur Chem. 147 (2016) 951–959, https://doi.org/10.1007/s00706-016-1678-x.